A two-dimensional waveguide beam for X-ray nanodiffraction
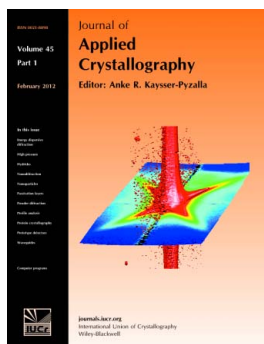
Christina Krywka, Henrike Neubauer, Marius Priebe, Tim Salditt, Jozef Keckes, Adeline Buffet, Stephan Volkher Roth, Ralph Doehrmann and Martin Mueller

Journal of Applied Crystallography covers a wide range of crystallographic topics from the viewpoints of both techniques and theory. The journal presents papers on the application of crystallographic techniques and on the related apparatus and computer software. For many years, the *Journal of Applied Crystallography* has been the main vehicle for the publication of small-angle scattering papers and powder diffraction techniques. The journal is the primary place where crystallographic computer program information is published.

Crystallography Journals Online is available from **journals.iucr.org**

A two-dimensional waveguide beam for X-ray nanodiffraction

Christina Krywka,[a]* Henrike Neubauer,[b] Marius Priebe,[b] Tim Salditt,[b] Jozef Keckes,[c] Adeline Buffet,[d] Stephan Volkher Roth,[d] Ralph Doehrmann[d] and Martin Mueller[e]

[a]Institute for Applied and Experimental Physics, University of Kiel, Leibnizstrasse 19, D-24118 Kiel, Germany, [b]Institute for X-ray Physics, University of Göttingen, Friedrich-Hund-Platz 1, D-37077 Göttingen, Germany, [c]Montanuniversität Leoben, Department Materialphysik, Jahnstrasse 12/I, A-8700 Leoben, Austria, [d]HASYLAB am DESY, Notkestrasse 85, D-22603 Hamburg, Germany, and [e]Helmholtz Zentrum Geesthacht, Max-Planck-Strasse 1, D-21502 Geesthacht, Germany. Correspondence e-mail: krywka@physik.uni-kiel.de

The micro- and nanofocus X-ray scattering (MINAXS) beamline of PETRA III is equipped with two consecutively arranged endstations, the last of which is the nanofocus endstation. The first in-beam commissioning of the experimental equipment was successfully performed at the end of 2010, using two-dimensionally confining hard X-ray silicon waveguides with cross sections of 50 nm × 50 μm to 50 nm × 2 μm for nanobeam generation. A full characterization of the waveguide-generated beams was performed, giving values for the beam geometries, the transmission efficiencies of the waveguides and absolute fluxes. Along with these results a detailed description of the setup is presented in this paper. A first high-resolution nanodiffraction experiment on a nanocrystalline TiN hard coating was performed to verify the resolution of the nanodiffraction setup and to reveal the local gradients across the blasted TiN coating. In conclusion, the main concern is the availability of the nanobeam, how it was generated and the fact that a beam out of a two-dimensionally confining waveguide was used for diffraction experiments for the first time.

1. Introduction

With the onset of efficient focusing methods, the generation of X-ray beams with sub-micrometre cross sections has become feasible. Significant success has been achieved during the past decade with regard to the concentration of low-divergence hard X-rays from third-generation synchrotron radiation sources (*e.g.* 8–30 keV) onto ever smaller areas using refractive, reflective and diffractive optical elements. Because the wavelength is of the order of 1 nm it is physically possible to confine hard X-rays within a spot size of only a few nanometres (Bergemann *et al.*, 2003). Still, focusing of X-rays to a spot size close to the diffraction limit remains technically very challenging. Therefore, as the available beam flux densities at recent sources have increased by several orders of magnitude, the concept of generating nanosized beams using X-ray waveguide-based nanocollimation methods has become increasingly relevant. Here we demonstrate the applicability of a waveguide-generated nanobeam for diffraction methods. The first waveguides used for X-ray diffraction experiments (Müller *et al.*, 2000) were laterally extended layers of low-*Z* materials (*e.g.* C or polymers), sandwiched between substrate layers, hence confining the X-ray wavefield in only one direction. To distinguish this type from the channel-like waveguides used here, the latter are commonly referred to as two-dimensional waveguides. These provide a two-dimensional confinement and offer new possibilities for the exploitation of their unique properties (such as spatial and coherence filtering) in high-resolution X-ray diffraction experiments.

Considering the multiplicity of techniques that can be used to directly generate a sub-micrometre-sized X-ray focus (Fresnel zone plates, Kirkpatrick–Baez mirrors, multilayer Laue lens, nanofocusing Si lenses), the use of two-dimensional waveguides may not appear worthwhile. However, the optical properties of any of these optics either exhibit strong wavelength dependence or require a specific source-image geometry to be maintained. Waveguides, on the other hand, can be regarded as small-scale beam collimation with coherence filtering properties (Jarre *et al.*, 2005). Therefore, changes of wavelength or the source distance leave the waveguide-generated nanobeam mostly uninfluenced. Consequently, waveguides can be used at beamlines with a tunable energy range or in conjunction with exchangeable pre-focusing optics. Particularly, the combination with a powerful pre-focusing technique (such as those mentioned above) enables the exploitation of the waveguide's strongest benefit: the wide scalability of the waveguide-generated nanobeam. Its size is determined mostly by the dimensions of the waveguide

channel, with dimensions of down to 10 nm being feasible, *i.e.* a size that is very challenging or impossible to obtain with the aforementioned optics used alone.

The basic idea of a two-dimensional X-ray waveguide is analogous to hollow waveguides for microwaves as it relies on the formation of an X-ray standing wavefield within the guiding channel (Cedola *et al.*, 1999; Krywka & Müller, 2011). Divergent or focused radiation is coupled into the two-dimensional waveguide by illuminating the entrance of the waveguide, while at the waveguide exit the size of the exiting wavefield is constricted by the waveguide dimensions and is also a function of the number of modes that can propagate in the waveguide, which in turn is defined by the geometrical parameters and material properties.

In this work, we have performed a detailed characterization of the waveguide-generated beam and demonstrated its applicability to nanodiffraction methods using the setup available at the nanofocus endstation of the MINAXS beamline at PETRA III (Hamburg). The micro- and nanofocus X-ray scattering beamline (MINAXS, also referred to as P03) is equipped with two consecutively arranged experimental endstations, called the microfocus endstation (Roth *et al.*, 2007) and the nanofocus endstation. The nanofocus endstation described herein begins at a distance of about 97 m from the undulator source and is the last part of the beamline. The setup at the nanofocus endstation was developed and installed within a cooperation of the University of Kiel and DESY. The ultimate design objective of the nanofocus endstation is to routinely provide a monochromatic X-ray beam with a cross section of about 100 nm for diffraction experiments, *i.e.* small-angle and wide-angle X-ray scattering measurements (SAXS and WAXS) with a high coherence option and, among other features, using two-dimensional waveguides as beam-defining elements.

2. Experimental setup

A schematic of the layout of the MINAXS beamline showing the position of the nanofocus endstation is displayed in Fig. 1. The source (at 0 m) is at a canted undulator, and a large-vertical-offset do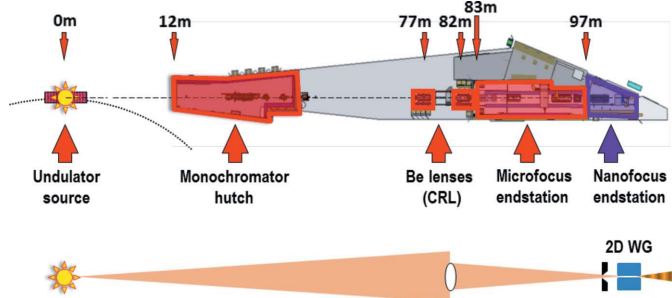uble Si(111) crystal monochromator is used to select a photon energy within the range of 8–23 keV, while higher-order harmonics are rejected by using Pd- or Mo-coated total external reflection mirrors. The here employed method to generate the sub-micrometre beam at the nanofocus endstation is based on X-ray waveguides and is performed in a two-step process. First, the source is imaged onto the waveguide position using compound refractive lenses (CRLs) with an apex curvature radius R of 200 μm (Lengeler *et al.*, 2005), installed in two lens exchangers located at 77 and 82 m from the source. To achieve a focal spot at the waveguide position (*i.e.* at 98.5 m from the source), one lens in the first exchanger and three lenses in the second exchanger were inserted. Subsequently, the radiation in the focal spot is coupled into a two-dimensional X-ray waveguide by illuminating its entrance opening, and the nanocollimated beam exiting the waveguide is used for experiments. This concept is shown schematically in Fig. 2.

A set of differently sized waveguides was used, fabricated next to each other into a single silicon wafer. Each of these waveguides is a hollow channel with a length of about 5.6 mm and different cross sections of 50 nm × 2 μm to 50 nm × 50 μm. Depending on the cross section, the separation between neighboring channels is 50–100 μm. The common length of 5.6 mm was chosen to best suit the used photon energy of 12.8 keV. Such an array of X-ray waveguides with two-dimensional confinement was first described by Pfeiffer *et al.* (2002), and in an improved form by Jarre *et al.* (2007). The guiding core of the first generation of waveguides consisted of a polymer, which was then overgrown with evaporated silicon as a cladding. More recently, the design scheme was extended to air-filled channels, defined by an electron lithography mask, transferred into silicon by reactive ion etching, and sealed by wafer bonding (Giewekemeyer *et al.*, 2010). These latter air-filled waveguides were used in the experiment described herein.

A more detailed scheme of the most important components constituting the experimental setup at the nanofocus endstation is shown in Fig. 3. The positioning of both the waveguide and the sample is based on a hexapod, giving the ability to
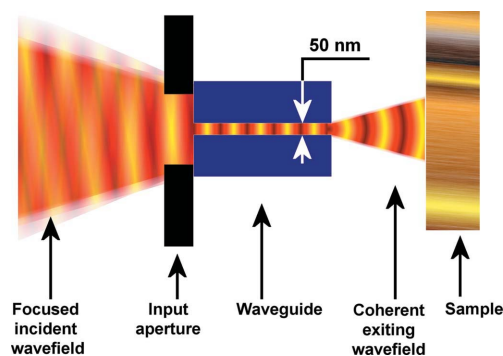

Figure 1
Schematic layout of the MINAXS beamline, showing the position of the nanofocus endstation and the relevant optical elements [Be lenses (CRL) = beryllium compound refractive lenses, 2D WG = two-dimensional X-ray waveguide]. The lower diagram shows a strongly simplified representation of the layout of the focusing geometry.

Figure 2
Schematic layout of the two-dimensional X-ray waveguide-based diffraction experiment: the prefocused X-ray wavefield is coupled into the waveguide (cross sections 50 nm × 2 μm to 50 nm × 50 μm). A spatially and coherently filtered wavefield propagates along the waveguide and the exiting beam illuminates a sample placed close (typically 100 μm) to the waveguide exit.

tune all six degrees of freedom (three linear, three rotational) with only one device. Both hexapods are equipped with top-mounted two-dimensional piezo-positioners, providing a translational reproducibility of down to 10 nm. In order to perform a high-resolution X-ray diffraction experiment, a flat thin sample is placed normal to the beam direction and very close to the exit of the waveguide (typical distance ∼100 μm). It is then scanned across the waveguide beam while diffraction images are recorded by means of a two-dimensional detector. Two long-working-distance telecentric video microscopes installed at orthogonal directions ease the sample alignment. A visible laser microbeam (spot diameter ∼100 μm) can be switched into the X-ray beam path and can also be used in conjunction with the video microscopes to ease the pre-alignment of samples and waveguides. Waveguide beam profiles as well as diffraction patterns were recorded using a pixel detector with single-photon characteristics (Dectris Pilatus 300K). Optionally, a CCD detector is also available at the nanofocus endstation of the MINAXS beamline. For measurements of the absolute beam flux a PIPS diode
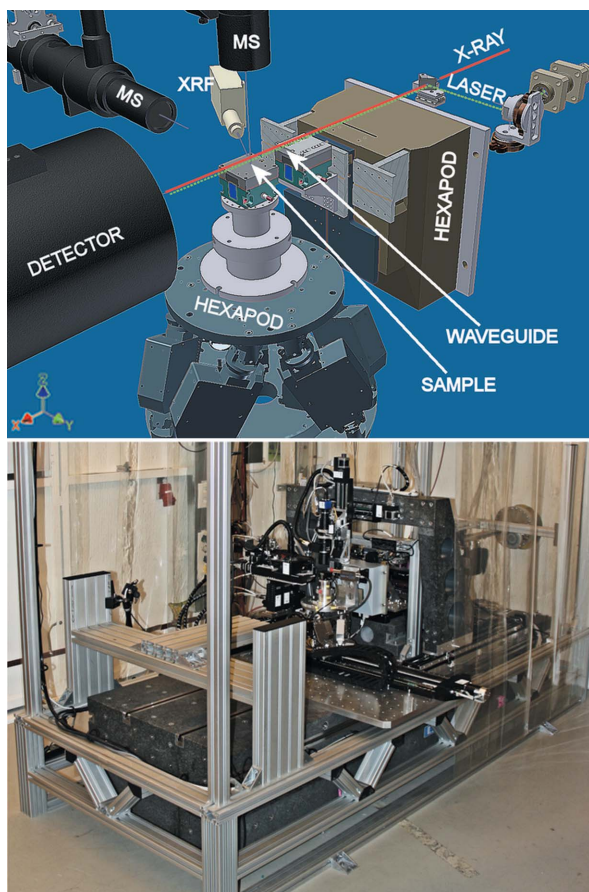

Figure 3
Top: schematic arrangement of the most important components that constitute the experimental setup at the nanofocus endstation (MS = microscope, XRF = X-ray fluorescence detector). Owing to their small size, the positions of the waveguide and of the sample are only indicated with arrows. Bottom: photograph of the current setup at the nanofocus endstation of the MINAXS beamline. The size of the granite table is 2.5 × 0.8 m. The beam direction is from right to left and the detector is removed for a better visibility of the setup.

(passivated implanted planar silicon diode, Canberra CAM-300AB) was used. To minimize the amplitude of externally and internally generated vibrations the entire setup is installed on a low-profile granite table (see photograph in Fig. 3).

3. Direct-beam characterization

Before X-ray waveguide-based measurements were commenced, an initial characterization of the beam delivered to the nanofocus endstation was performed. The size of the beam focused by the CRLs (long-focal-distance mode) was determined through horizontal and vertical slit scans, each with a slit opening of 10 μm, using the PIPS diode. The horizontal and vertical profiles were each fitted with a single Gaussian, yielding a beam size of 116 × 80 μm (horizontal × vertical, FWHM) in the CRL focus. The beam divergence in the CRL-focused beam was calculated from the beam size, the focal length and the effective aperture of the compound lens system using *CRLCALC* (Version 5.0, http://newton.phy. tu-dresden.de/applets/crlcalc.html) to be below 0.1 mrad. For the absolute photon flux in the focal spot a value of $N_0 = 3.5 \times 10^{11}$ s^{-1} was measured (at a storage ring current of 100 mA). N_0 was calculated from the PIPS-diode current I_{PIPS} using

$$N_0 = \frac{I_{PIPS} \varepsilon_{Si}}{eE} \frac{1}{1 - \exp(-W/\alpha_{Si})}, \qquad (1)$$

where ε_{Si} is the ionization energy for silicon (3.61 eV), e is the electron charge (1.602 × 10^{19} C) and E is the incident photon energy (12.8 keV). The second coefficient is the inverse of the fraction of radiation absorbed within the depletion thickness W of the reverse-biased PIPS diode and α_{Si} is the attenuation length of silicon.
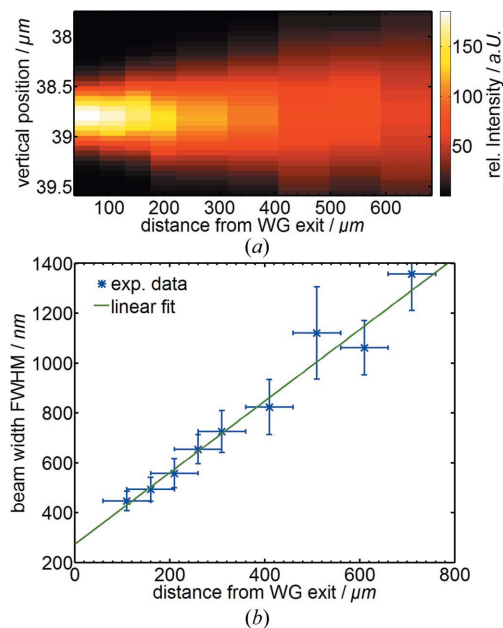

Figure 4
(*a*) Vertical cross section of the waveguide (WG) beam, calculated from the derivatives of a knife-edge scan series. (*b*) Full width at half-maximum (FWHM) values of the vertical cross section as a function of the distance from the waveguide exit.

4. Waveguide-beam characterization

Radiation is coupled into the waveguide by illuminating the entrance of the waveguide, which is aligned to coincide with the X-ray beam. The portion of radiation that over-illuminates the entrance of the waveguide is adsorbed in the substrate material. As mentioned before, the waveguides used here were all fabricated into one silicon wafer, arranged next to each other. This way, if one waveguide channel is precisely aligned, the selection of a specific waveguide channel can be achieved by simply translating the wafer laterally. The in-beam alignment procedure of a two-dimensional waveguide involves four degrees of freedom (two translational, two rotational), which have to be precisely set within typically 10 µm and 1 mrad, respectively. The use of hexapods with freely definable pivot points combined with a two-way microscope observation significantly facilitates this procedure and enables an unprecedented flexibility of the alignment at the nanofocus endstation. An example is the two-dimensional rotation of a waveguide channel around a pivot point specifically set to coincide with the waveguide's input opening (see below).

4.1. Waveguide-beam profile

To record the geometry of the beam exiting the waveguide a series of vertical knife-edge scans were performed at increasing distances. The derivatives of the knife-edge scans recorded from the smallest waveguide channel (50 nm × 2 µm) are shown in Fig. 4(a). The vertical step size in the scans was 50 nm, and two different probes were used as knife edges to better account for their unspecified nano-roughnesses: a discarded tungsten slit blade (3 mm thick) and a lithographically fabricated gold transmission electron microscope slit (30 µm thick, obtained from Plano GmbH, Germany). *In situ* microscope images of the knife edges aligned closely to the waveguide exit are shown in Fig. 5, recorded with the horizontally viewing video microscope. The distance between
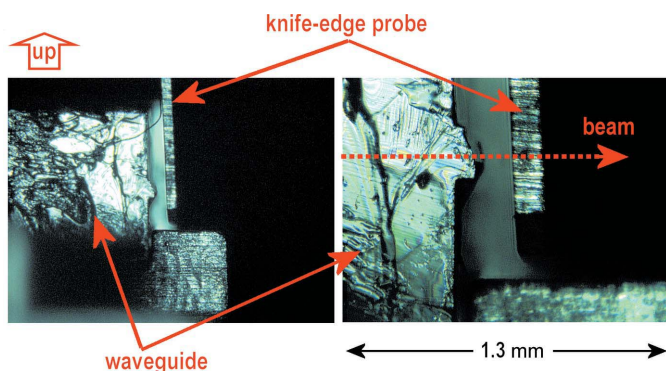
the waveguide exit and the knife-edge probe was determined as follows: First the parallel-aligned knife-edge probe was carefully approached until it visibly touched the silicon wafer of the waveguide, marking the closest possible approach. This minimum distance was estimated from the calibrated microscope image, on the basis of the side faces visible in the microscope image. For this minimum distance an error of ±50 µm must be assumed because of the irregularly shaped and slightly angled contour of the breaking edge stud, in which the actual waveguide channel ends (see Fig. 5). Then, the distance was increased with a calibrated positioner and knife-edge scans were performed at each position. The results of the two different knife-edge probes are in good accordance, so only data from one type (tungsten slit blade) are shown in Fig. 4. Evidently, the beam diameter increases almost linearly with the distance from the waveguide exit, the smallest measured width being 446 (39) nm at a distance of 110 (50) µm. From the linear increase of the beam width the vertical size of the beam at the waveguide exit (*i.e.* at zero distance) can be calculated by extrapolation, yielding a value of 273 (68) nm. This value is significantly larger than the vertical dimension of the waveguide (50 nm), determined by means of electron microscopy. However, the roughness of the knife-edge probes on the sub-micrometre scale was indeterminate and must therefore be regarded as the main source of this deviation. Also, vibrations (of the order of 100 nm in amplitude) of the lever holding the knife-edge probe could not easily be mitigated during the experiment.

4.2. Waveguide-beam divergence

From the linear fit a beam-width increment of 1.4 (2) nm µm^{-1}, *i.e.* a divergence of 1.4 (2) mrad, was obtained. This value is significantly lower than the critical angle of total external reflection α_c, which is approximated by (Als-Nielsen & McMorrow, 2001)

$$\alpha_c \simeq (2\delta)^{1/2}, \tag{2}$$

where $\delta = 2.972 \times 10^{-6}$ is the dispersion from the complex index of refraction for silicon at an incident photon energy of 12.8 keV, calculated using the CXRO X-ray database (Gullikson, 2011). Hence α_c is estimated to be 2.44 mrad. This is an upper limit for the opening angle of the exit beam. More precisely, the full width of the opening angle α is calculated by a Fourier transform of the near-field intensity distribution in the exit plane of the waveguide. For a 50 nm waveguide the fundamental mode has a width of $\Delta = 41.8$ nm (FWHM). Approximating the line shape by a Gaussian, and using the analytical formula derived for a Gaussian beam,

$$\alpha = 4\ln(2)\lambda/\pi\Delta, \tag{3}$$

a far-field diffraction cone of $\alpha = 2.0$ mrad is obtained. This has to be compared with the experimental value of 1.4 (2) mrad, which points to the fact that the near-field distribution is broadened by higher-order modes, as expected from finite difference simulations.

Figure 5
Pictures of the knife-edge probe aligned close to the exit of a two-dimensional waveguide. The images were recorded at different magnifications using the horizontally viewing video microscope (see Fig. 3) and the X-ray beam direction is from left to right. The stud through which the beam exits the waveguide protrudes about 100 µm from the waveguide face side and is a breaking edge caused by the waveguide fabrication process. The dotted line indicates the position of the waveguide channel in the silicon wafer (the actual waveguide channel runs within the silicon, *i.e.* is not visible in the images).

4.3. Waveguide transmission efficiency

In order to determine experimentally the transmission properties of the waveguide channels, the ratio of the flux illuminating the waveguide *versus* the flux exiting a specific channel was measured for all waveguide sizes. For this purpose, the fraction of the primary beam transmitted through the waveguide was determined (effective waveguide acceptance A_{eff}) and compared with the calculated highest possible acceptance A_{max}.

The exiting flux was determined using the same method as previously described for the direct beam, but to prevent the illumination of more than one waveguide channel at a time, the incident CRL-focused beam was horizontally collimated and data were recorded using different slit openings (10–40 μm). Additionally, to block the direct-beam air scattering a 400 μm tungsten pinhole was located in front of the waveguide. The values for A_{eff} measured for all waveguide channel sizes are shown in Fig. 6(a). Differently sized slit openings were used for all waveguide sizes. Obviously, A_{eff} increases with larger slit opening, which is intuitive for the largest waveguide channel (50 μm × 50 nm) where the slit opening width is generally smaller than the channel width. For the smaller sized channels (25 μm × 50 nm, 10 μm × 50 nm and 2 μm × 50 nm), on the other hand, the over-illumination of the

channel input becomes important. The transmission of the silicone substrate surrounding a waveguide channel is $T = 1.6 \times 10^{-9}$ (for 5.6 mm Si at 12.8 keV). While it is marginal for the 25 μm × 50 nm channel, the amount of flux transmitted through the silicone substrate is no longer negligible for the smaller channels when they are illuminated with a beam that is many times wider than the channel opening. In this case A_{eff} is increased as the transmitted fraction of the beam contributes to the flux measured at the waveguide exit. Therefore, the most reliable A_{eff} values are those measured with the slit opening width best fitting the waveguide channel width. For technical reasons, the slit opening width could not be decreased below 10 μm, which is why the true value of A_{eff} for the 2 μm × 50 nm channel must be considered to lie below the lowest displayed marker. It must be noted that the relatively low values of A_{eff} shown here (of the order of 10^{-4}–10^{-6}) are in general a result of the very large size of the incident beam as compared to the vertical waveguide cross sections (50 nm), *i.e.* they do not reflect a low transmission efficiency within the waveguide channels.

Also shown in Fig. 6(a) are the calculated highest possible waveguide acceptances A_{max}. Here, the fractions of the incident CRL beam selected by the waveguides are taken into account and a lossless propagation within the channels is assumed. These values were calculated from the fractions of the Gaussian beam profile integrals corresponding to the horizontal and vertical widths of a waveguide channel (w_h and w_v, respectively):

$$A_{max} = \left\{ \int_{-w_h/2}^{w_h/2} \exp\left[-\left(\frac{x}{0.85 \mathrm{FWHM}_h} \right)^2 \right] dx \right.$$
$$\left. \times \int_{-w_v/2}^{w_v/2} \exp\left[-\left(\frac{y}{0.85 \mathrm{FWHM}_v} \right)^2 \right] dy \right\}^{-1} . \quad (4)$$

Here, $\mathrm{FWHM}_{h,v}$ are the experimentally determined horizontal and vertical half-widths of the CRL-focused beam. For a given waveguide channel size the value $T_{est} = A_{eff}/A_{max}$ (where A_{eff} is measured with the best-fitting slit opening width) is the ratio of the measured acceptance over the calculated one in which a lossless propagation was assumed. Consequently T_{est} reflects the true transmission efficiency of the wavefield propagation along the waveguide channel. For the differently sized channels T_{est} is shown in Fig. 6(b) and the increase of T_{est} reflects the increase of the geometric cross section in the horizontal direction. As the measurement of the acceptance of the 2 μm × 50 nm channel was distorted by over-illumination effects (see above), the corresponding values of T_{est} are higher than expected. However, from the absolute transmission efficiency values (10–30%) it is evident that, with a sufficiently strong focused incident beam illuminating the waveguide channel input, a similarly high fraction of the incident flux can be recovered in the beam exiting the waveguide.
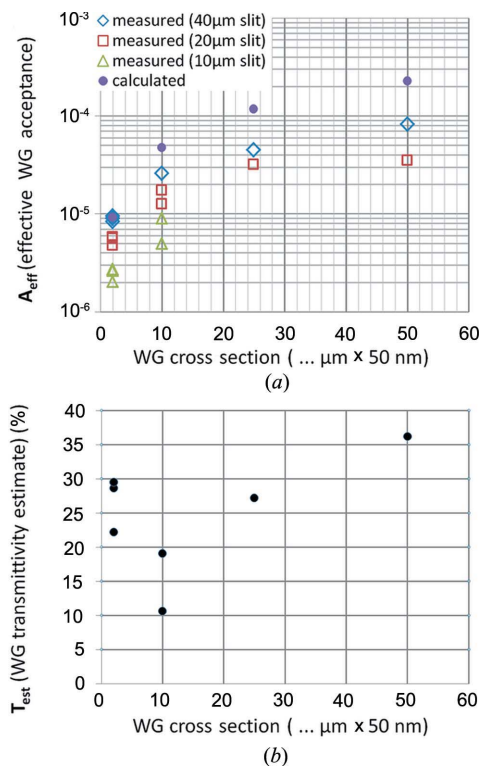
Figure 6
(a) Experimentally determined flux acceptances A_{eff} of the different waveguide channels and theoretical values assuming a lossless propagation within the waveguides. All available waveguide sizes (50 nm × 2 μm to 50 nm × 50 μm) were investigated. The incident beam was collimated horizontally using multiple slit openings (10–40 μm). (b) Estimation of the actual transmission efficiencies (T_{est}) within the waveguide channels, using the flux acceptances measured at a collimation best matching the waveguide width.

Christina Krywka et al. · Two-dimensional waveguide beam

4.4. Tilt acceptance of the waveguide

The use of hexapods as primary aligning elements enabled us to perform precise scans of the waveguide channel tilt angles with respect to the X-ray beam direction. For this purpose the pivot point of the hexapod was set to coincide with the entrance of a specific waveguide channel, as shown schematically in Fig. 7, so that rotations around the φ axis and the χ axis could be performed without unwanted movement of the channel entrance. It is worth mentioning that these scans could be initiated *ad hoc*, *i.e.* requiring no mechanical adaptions, simply by using three-dimensional computer-aided design software to deduce the precise positions of the waveguide channels in the coordinate system of the hexapod and a subsequent video-microscope-based optimization.

Scans were performed around both axes (φ and χ) within a typical range of $\pm 0.1°$ around the orientation previously identified to be the optimum alignment, *i.e.* with the beam direction and channel axis collinear ($\varphi = 0°$ and $\chi = 0°$). The detector (Dectris Pilatus 300K) was installed at a distance of 2.4 m from the waveguide and images of the waveguide beam were recorded while the angles were scanned. To reduce air scattering a vacuum flight tube was installed between the waveguide and the detector. A far-field image of the 50 μm × 50 nm waveguide beam is shown in Fig. 7 (middle panel, $\varphi = 0°$) with its typical vertically elongated structure reflecting the strong confinement of the beam in the vertical direction (*i.e.* the smaller, 50 nm dimension). In the horizontal direction the beam is much less divergent, according to the waveguide's larger horizontal dimension (50 μm) and the resulting weaker beam confinement. As indicated by the example image taken at $\varphi = 0.1°$, the geometry of the beam significantly changes when the φ-tilt angle is different from zero (zero corresponding to optimal angle, *i.e.* the waveguide is parallel to the X-ray beam). The most prominent effect is the occurrence of sharply separated additional side maxima, while the position of the primary waveguide beam portion remains constant. The quantity as well as the horizontal separation of the side maxima was found to be correlated with the φ-rotation angle. Shown in the right panel of Fig. 7 is a composition of the vertical projections of far-field images recorded in a φ scan within a range of $\pm 0.1°$ with a step size of $\Delta\varphi = 0.002°$ (*i.e.*

every horizontal pixel line corresponds to a far-field image reduced to its x-axis projection). Evidently, there is strong intensity localization for the central beam and its first-order maximum. It was found that, given a precisely aligned waveguide, the angle corresponding to the separation of the central beam and its first-order maximum equals 2φ, *i.e.* the first-order side maximum can be identified as the portion of the waveguided beam that is totally reflected on the inner side wall (50 nm height) of the waveguide channel, inclined by the tilt angle φ. The higher-order side maxima can be explained by interference effects occurring between the primary waveguide beam and its reflected portion.

A rotation around the χ axis, on the other hand, does not produce a similar effect. Instead, only a slight vertical shift of the far-field image occurs when the χ-rotation angle is increased, leaving the geometry of the far-field image basically unchanged. It is assumed that the reflected part of the beam is then superimposed with the vertically extended primary waveguide beam, leaving the reflected part difficult to observe. For both the φ and the χ rotation, the exiting beam disappears as soon as a specific angle is exceeded, being largest for the widest waveguide. For the widest waveguide channel this angle corresponds to the critical angle of grazing incidence α_c, while for the narrower channels a smaller angle is observed.

In summary, taking into account the high coherent fraction of radiation constituting the waveguide beam, experimental applications must be considered in order to exploit the here demonstrated precise tuneability of the waveguide beam horizontal separation (*e.g.* for coherent X-ray diffraction methods where two coherent, closely separated beams are used).

4.5. Nanodiffraction on TiN hard coating

Among the first experimental approaches to use the sub-micrometre spatial resolution provided by the waveguide-generated nanobeam was a nanodiffraction experiment on a nanocrystalline TiN coating. Because of their high hardness and wear resistance, protective polycrystalline TiN hard coatings are used in various machining applications, especially for metal cutting or turning (Mayrhofer *et al.*, 2006). The lifetime and the performance of the coated tools depend decisively on the local gradients of microstructure and residual stress across the hard coatings (Korsunsky *et al.*, 2010; Massl *et al.*, 2007). TiN coatings on WC/Co substrates deposited using chemical vapor deposition (CVD) usually possess unfavorable tensile in-plane residual stresses, which can be turned to compressive ones by using a post-deposition surface treatment like blasting (Klaus *et al.*, 2008; Bartosik *et al.*, 2011). The aim of the experiment was to verify the resolution of the nanodiffraction setup and to reveal the
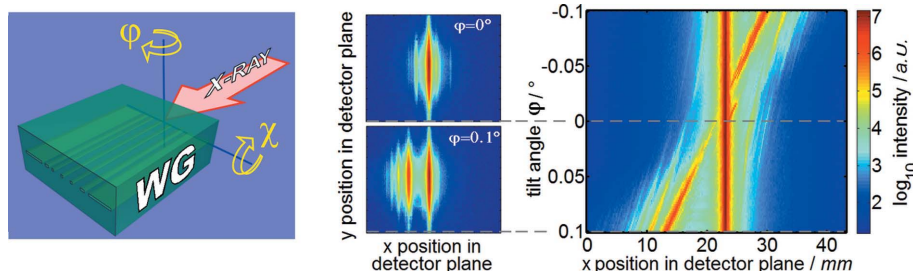
Figure 7
Left: schematic view of the waveguide (WG) tilt scan, performed around axes set to coincide with the channel entrance. Middle: two example far-field images of the beam from a 50 μm × 50 nm waveguide, recorded at different φ-tilt angles (detector distance of 2.4 m). The dashed lines indicate where the vertical projections of these images are located in the tilt angle plot (right), composed of projections of images recorded within a φ-tilt angle range of $\pm 0.1°$. Note the logarithmic intensity scaling in all images.

local gradients across the blasted TiN coating. A polycrystalline 6 μm-thick TiN coating, serving as a model system, was deposited on WC/Co substrates using a CVD process at 1173 K, applying N_2, H_2 and $TiCl_4$ as reactant gases. The as-deposited coating was blasted using a pressure of 3×10^5 Pa applying Al_2O_3 particles with a diameter of approximately 50 μm (Klaus *et al.*, 2008). From the coating/substrate composite, a 10 μm-thick slice was prepared by cutting the composite perpendicular to the interface, by mechanical polishing using a diamond saw and finally by focused-ion beam milling.

The 10 μm-thick slice was characterized in transmission WAXS geometry (wavelength $\lambda = 0.0969$ nm) by scanning the waveguide beam vertically across the horizontally aligned coating and the substrate using a vertical step size of 0.2 μm. The sample was positioned at a distance of about 100 μm from the 50 μm $\times$ 50 nm waveguide. The setup is shown schematically in Fig. 8. For every measurement step, one quadrant of a Debye–Scherrer ring was collected at a sample–detector distance of 120.4 mm. The rings were analyzed using the *Fit2D* software package (Hammersley *et al.*, 1996) by evaluating the diffraction intensity as a function of the diffraction angle 2θ.

In Fig. 8 the distribution of the experimentally observed intensities as a function of the diffraction angle and the vertical scanning position is presented in a composite image constructed from the individual Debye–Scherrer rings. At vertical positions down to about 7.5 μm, one can recognize TiN 111 and TiN 200 reflections. The varying intensity along the TiN reflections indicates the presence of a strong crystallographic texture in the coating. The relative changes of the peak positions (marked by arrows) can be interpreted as the presence of compressive strains, which are obvious especially close to the blasted coating surface. Though the coating was thinned to a 10 μm slice and a part of the macroscopic (first-order) strains probably relaxed, the changes in the peak positions indicate that a portion of strain was still preserved in the coating. Moreover, one can expect that the blasting did not

affect the residual stress state at the interface. At vertical positions of about 7.5–8 μm, a WC 100 reflection can be observed at about $2\theta = 22°$, together with a higher background caused probably by the X-ray fluorescence.

In summary, the X-ray nanodiffraction experiment revealed microstructure and strain gradients across the coating with a sub-micrometre resolution. In future, the approach will be used to analyze compositionally graded thin films and coatings in order to understand the correlation between processing parameters (like deposition conditions, temperature history) and the actual microstructure and strain depth profiles.

5. Conclusions

The feasibility of an X-ray beam generated by a two-dimensionally confining waveguide for nanodiffraction experiments is demonstrated for the first time, continuing the applicability studies on one-dimensionally confining waveguides for microdiffraction (Müller *et al.*, 2000). Data were recorded at the nanofocus endstation of the MINAXS beamline at PETRA III. Although in principle this method of nanocollimation is also applicable to a laboratory source, for the waveguided beam to obtain the flux density required for the diffraction experiments presented here, a microfocused synchrotron beam is essential.

Waveguides with cross sections of 50 nm $\times$ 2 μm to 50 nm $\times$ 50 μm were employed, using a CRL-focused beam to front-couple radiation into the waveguide. The high width-to-height aspect ratio of the waveguide cross section was chosen to compensate for the high over-illumination of the waveguides by the relatively large size of the prefocused beam. A vertical beam size of 237 nm was measured at the exit of the smallest waveguide with a vertical beam divergence of 1.4 mrad. The transmission efficiencies of the waveguide channels were determined to be of the order of 10–35%, depending on the cross section of the waveguide channels. The significant facilitation of precise (waveguide) alignments using hexapods is pointed out. By precisely tilting the waveguide around a pivot point set to coincide with the channel input, a distinct tuneable beam splitting was observed that could be attributed to a reflection of radiation on the inner wall of the waveguide channel. Using this approach for nanobeam generation, high spatial resolutions are achievable, limited only by the size of the waveguide channel cross sections. To verify the resolution of the setup, an X-ray nanodiffraction experiment was performed on a TiN coating on a WC–Co substrate. The data revealed microstructure and strain gradients across the coating with a sub-micrometre resolution.

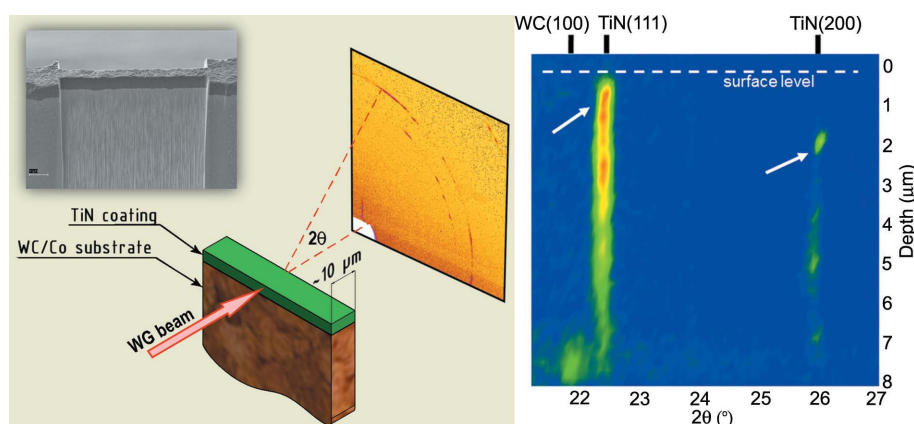In future, smaller waveguides with a less elongated cross section, *i.e.* a width-

Figure 8
Left: schematic setup of the nanodiffraction experiment on a TiN coating deposited on a WC–Co substrate (inset shows a transmission electron microscope image of the actual sample). Right: composite image of the experimentally observed intensities recorded in the nanodiffraction experiment. The intensity modulations of the TiN 111/200 and substrate WC 100 reflections indicate the presence of a strain gradient within the microstructure of the coating.

to-height aspect ratio close to 1, can be used because of the currently ongoing implementation of a Kirkpatrick–Baez (KB) mirror optics at the nanofocus endstation of MINAXS. By providing a nanofocused beam, the mirror optics will minimize the over-illumination of the waveguides and provide the benefits of both a reflective mirror optics and coherent radiation from X-ray waveguides. These benefits can be exploited for nanodiffraction experiments and, as a result of the longer working distances of the KB mirrors, for nano grazing-incidence SAXS experiments (Roth *et al.*, 2011).

References

Als-Nielsen, J. & McMorrow, D. (2001). *Elements of Modern X-ray Physics.* New York: Wiley.
Bartosik, M., Pitonak, R. & Keckes, J. (2011). *Adv. Eng. Mater.* **13**, 705–711.
Bergemann, C., Keymeulen, H. & van der Veen, J. F. (2003). *Phys. Rev. Lett.* **91**, 204801.
Cedola, A., Fonzo, S. D., Jark, W., Lagomarsino, S. & Soullié, G. (1999). *J. Phys. D Appl. Phys.* **32**, A179.
Giewekemeyer, K., Neubauer, H., Kalbfleisch, S., Kruger, S. & Salditt, T. (2010). *New J. Phys.* **12**, 035008.
Gullikson, E. (2011). *CXRO X-ray Interactions With Matter*, http://henke.lbl.gov/optical_constants/.
Hammersley, A., Svensson, S., Hanfland, M., Fitch, A. & Hausermann, D. (1996). *High Pressure Res.* **14**, 235–248.
Jarre, A., Fuhse, C., Ollinger, C., Seeger, J., Tucoulou, R. & Salditt, T. (2005). *Phys. Rev. Lett.* **94**, 074801.
Jarre, A., Seeger, J., Ollinger, C., Fuhse, C., David, C. & Salditt, T. (2007). *J. Appl. Phys.* **101**, 054306.
Klaus, M., Genzel, C. & Holzschuh, H. (2008). *Thin Solid Films*, **517**, 1172–1176.
Korsunsky, A., Sebastiani, M. & Bemporad, E. (2010). *Surf. Coat. Technol.* **205**, 2393–2403.
Krywka, C. & Müller, M. (2011). *X-ray Diffraction: Modern Experimental Techniques*, edited by O. H. Seeck & B. Murphy. Singapore: Pan Stanford Publishing.
Lengeler, B., Schroer, C. G., Kuhlmann, M., Benner, B., Florian Günzler, T., Kurapova, O., Zontone, F., Snigirev, A. & Snigireva, I. (2005). *J. Phys. D Appl. Phys.* **38**, A218.
Massl, S., Keckes, J. & Pippan, R. (2007). *Acta Mater.* **55**, 4835–4844.
Mayrhofer, P., Mitterer, C., Hultman, L. & Clemens, H. (2006). *Prog. Mater. Sci.* **51**, 1032–1114.
Müller, M., Burghammer, M., Flot, D., Riekel, C., Morawe, C., Murphy, B. & Cedola, A. (2000). *J. Appl. Cryst.* **33**, 1231–1240.
Pfeiffer, F., David, C., Burghammer, M., Riekel, C. & Salditt, T. (2002). *Science*, **297**, 230–234.
Roth, S., Autenrieth, T., Grubel, G., Riekel, C., Burghammer, M., Hengstler, R., Schulz, L. & Muller-Buschbaum, P. (2007). *Appl. Phys. Lett.* **91**, 091915.
Roth, S., Herzog, G. *et al.* (2011). *J. Phys. Condens. Matter*, **23**, 254208.